Heliyon 10 (2024) e26842

Contents lists available at ScienceDirect

Heliyon

journal homepage: www.cell.com/heliyon

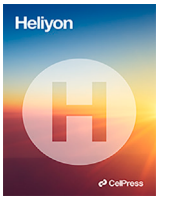

Research article

Highly sensitive refractive index sensing with a dual-band optically transparent ITO-based perfect metamaterial absorber for biomedical applications

Sumaia Jahan Mishu *, Muhammad Asad Rahman, Nipa Dhar

Department of Electrical and Electronic Engineering, Chittagong University of Engineering and Technology, Chattogram 4349, Bangladesh

ARTICLE INFO

Keywords:
Metamaterials
Refractive index sensor
Absorber
Sensitivity
Dual-band

ABSTRACT

In this paper, a dual-band optically transparent square-shaped perfect metamaterial absorber operating in the frequency range from 2 to 4 terahertz (THz) is proposed. The structure consists of an indium tin oxide (ITO)-based split ring resonator (SRR) structure with additional splits and rectangular inner strips to form the top layer over the lead glass substrate. Perfect absorption is attained in the frequencies of 2.089 and 3.892 THz with absorbances of 99.99% and 99.98% in TE polarization mode, respectively. Perfect absorption is also achieved in TM polarization mode at 2.23 THz. Broadband absorption is found in TM polarization mode with full width half maximum (FWHM) of 1.1742. The proposed structure has one polarization-insensitive band in TE polarization mode. Absorbance is greater than 80% and 90% in the successive absorption peaks even at 60° and 75° of incidence, respectively. The resonance frequency is sensitive to the refractive index of the medium. As a result, the proposed metamaterial structure may be implemented as a refractive index (RI) sensor with a high sensitivity of 1109 GHz/RIU and 1954 GHz/RIU in both absorption bands for a refractive index range of 1.34 to 1.40. It's interesting to note that the refractive index of most biological samples ranges from 1.3 to 1.39. The figure of merit (FOM) of the proposed sensor can reach as high as 10 and 14 for the 1st and 2nd frequency bands. As a result, the proposed sensor has a high sensitivity and can be employed in medical applications. Potential applications of the proposed absorber include imaging, biomedical sensing, etc.

1. Introduction

Electromagnetic (EM) metamaterials are a class of composite engineered materials having qualities that exhibit unusual electromagnetic phenomena not present in natural materials [1–4]. Researchers have researched it extensively for studying negative refractive index, super lenses, tiny wireless components [5–10], and absorbers [11–15], etc. because it offers many unusual strategies to manipulate light [16]. Solar cell enhancement, spectral imaging, non-destructive sensing, signature control, communications, and emissivity control are only a few of the applications for artificially manufactured electromagnetic absorbers. In addition to the above-mentioned structures, metamaterial absorbers made up of distinct electric and/or magnetic resonators have piqued the interest

* Corresponding author.
E-mail address: u21MEE026P@student.cuet.ac.bd (S.J. Mishu).

https://doi.org/10.1016/j.heliyon.2024.e26842
Received 3 September 2023; Received in revised form 15 February 2024; Accepted 20 February 2024

Available online 28 February 2024

of many researchers. metamaterial structures with a dielectric substrate constitute the majority of perfect metamaterial absorbers [17,18]. The perfect metamaterial absorber has a wide range of applications, including spectroscopic detectors [19], thermal imaging [20], and optical devices [21].

In the fast-increasing field of terahertz (THz)-based technologies [22,23], the development of perfect absorbers has recent times been a major issue of interest [24,20]. The frequency interval between 0.1 THz to 10 THz is referred to as THz waves. Since the first generation of perfect absorbers was devised by Landy et al. [25], perfect absorber development has progressively become a widely discussed topic. In 2008, Tao et al. [26] reported the first metamaterial absorber in the THz frequency regime, providing a perfect absorbance of 98% at 1.12 THz, based on numerical and experimental characterization. A metamaterial with a high effective medium ratio is presented for S-band and X-band microwave applications, with absorptances of 99%, 98%, and 81%, respectively, at 4.27 GHz, 5.42 GHz, and 12.40 GHz [27]. For an incident angle up to 80 degrees, this scientific study proposes a resonator that delivers over 99% absorbance for all polarization angles, with 70% and 93% efficiency for TE and TM polarized waves, respectively [28]. This paper shows a modified penta-band SRR-based meta-atom absorber with five distinct resonant frequencies in the microwave regime, covering the S, C, X, and Ku bands [11].

The suggested absorber's resonant frequencies can be modified by adjusting the chemical potential for a triple-band and a quad-band absorber while maintaining over 80% absorption [29]. At 2.44 THz, an ultra-narrow perfect metamaterial absorber with an absorbance of 99.49% and a high quality-factor value is proposed in this study for refractive index sensing applications [30]. In the 6.6-8.9 THz region, an ultra-wideband THz perfect metamaterial absorber with over 99% perfect absorption has been developed in this study [13]. Second, phase change material VO_2 was incorporated into the absorber to enhance the functionality, and three tunable THz metamaterial absorbers based on VO_2 were constructed, enabling broadband movement and multi-band conversion. In [31], a new all-metal metamaterial absorber is suggested. At 1.563 THz, this absorber can reach 99.95% absorption. Padilla et al. [32] designed a metamaterial that comprised a periodic array of metallic resonator, dielectric, and a ground plane (to inhibit EM radiation transmission) to demonstrate the earliest metamaterial absorber to show perfect absorption in the infrared regime with an exceptional absorbance of 97%. Using the surface plasmon approach, in [33], a polarization-insensitive broadband metamaterial absorber is suggested, which exhibits near unit absorbance in the visible regime, with possible usage in solar cells, thermal imaging, etc. In [34], a titan-based resonator is studied for near-perfect solar radiation absorption across the entire spectrum. The average absorbance of the absorber is up to 93.17%.

In [35], a novel perfect metamaterial absorber comprised of a dielectric and metal structure is investigated, which can excite resonance in the visible regime with a narrow absorption bandwidth and a high quality-factor while exhibiting angle and polarization independence. Furthermore, when used as a refractive index sensor, it achieves a significant maximum sensitivity and figure of merit (FOM). A metamaterial absorber based on a metallic square structure is simulated in [36], confirming that the highest absorption is about 97.8% on average at multiple distinct frequencies and that the absorption spectra can be actively controlled by varying the medium temperature. The InSb dielectric gap layer, whose permittivity may be altered by changing the temperature, must be filled into the structure. For monitoring protein concentration, a four-resonator-based metamaterial THz biosensor produced by a surface micromachining approach is described in [12]. The developed biosensor is easy to use and highly sensitive without requiring rigorous experimental conditions, which is critical for biomolecule identification and medical diagnostics. This study [37] designed and developed a polarization-insensitive metamaterial biosensor that determined the minimal sensing concentration and sensitivity for bovine serum albumin detection. For the purpose of identifying the severe acute respiratory syndrome-CoV-2 nucleic acid, integration of the photothermal effect with plasmonic sensing transduction was conducted here [38] to create a dual-functional biosensor.

In this paper, a THz metamaterial absorber with perfect absorption has been proposed. Dual-band absorption is achieved by this metamaterial absorber with perfect absorption in both. It performs well in terms of absorption in both TE and TM polarization modes. Moreover, the metamaterial perfect absorber has a high tolerance for incidence and polarization angle in both TM and TE modes, and they can exhibit perfect dual-band absorption across a wide range. The performance for refractive index sensing is simulated using a step size of 0.005 refractive index unit (RIU). The structures FOM as a biomedical sensor can reach as high as 10 and 14 for 1st and 2nd absorption peaks, respectively. The structure is simple in its design. Implementing a simple, planar form is an excellent example of mitigating the complexities associated with an intricate structure, such as material compatibility, control over feature size, complex mask production, integrating multiple procedures, etc., which is a significant disadvantage in fabrication [12]. Also, as the structure is glass-based, it may provide a seamless integration with consumer devices, as they are excellent candidates for THz devices and circuits [39]. They also can consolidate THz systems onto a single chip or substrate. They can earn greater yield at lower manufacturing expenses for large-scale production, which is required to lower total production costs per unit while maintaining excellent performance in comparison to conventional semiconductor rivals such as GaAs and InP technologies. Furthermore, because the ITO transparent layer is employed as a top layer and enables optical detection and non-invasive monitoring, among other features, it is more appropriate for use in biomedical applications [40]. Since, the entire structure's transparency allows for real-time monitoring and analysis of biological processes, this is especially useful in applications like optical biosensors, where it makes the procedure safer and less disturbing for the individual or sample. Additionally, the refractive indices of biomedical samples range from 1.3 to 1.39 [41]. In particular, blood and malignant cell organelles have refractive indices within the range of 1.35 to 1.39 [42]. As a result, implementing a sensor that operates in this range and has excellent sensitivity and resolution could be extremely useful for diagnosing malignancies, carcinoma, and other diseases. Therefore, it can be concluded that the study is advantageous in many different prospects, starting from manufacturing, consumer production, biomedical detection, etc.

The study is organized in the described manner: the structural design of the proposed absorber is described in the first section, followed by the simulation results in the next part. Then, electric field, magnetic field, and surface current distribution plots offer

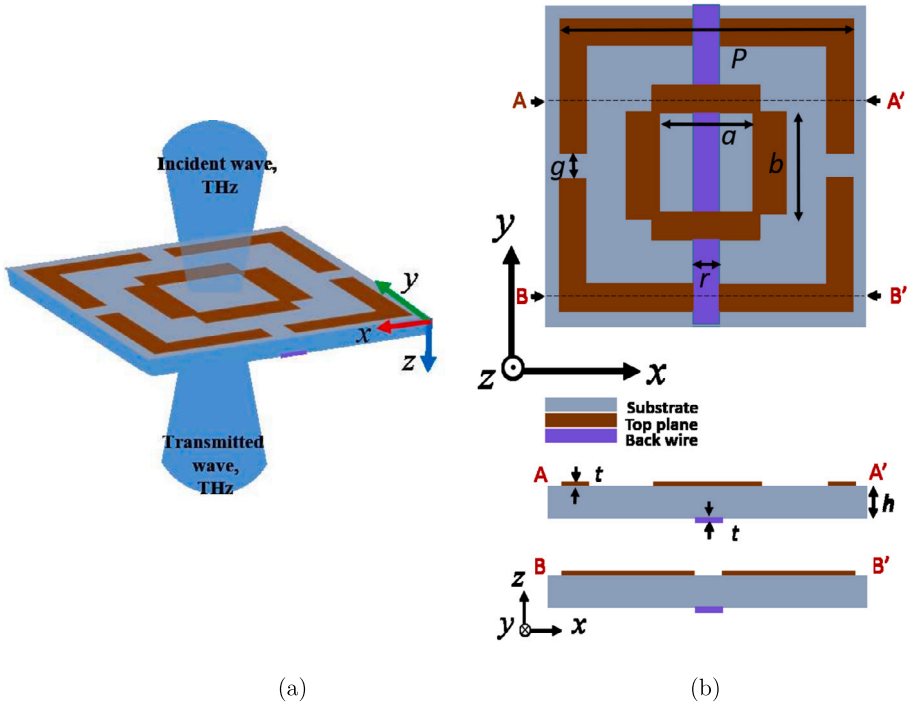

Fig. 1. (a) Simulation arrangement and (b) structural pattern of the proposed metamaterial absorber.

a detailed examination of the appearance of absorption peaks. A parametric analysis is also performed to support the parameter selection and tolerance, and the following section discusses the sensitivity and efficiency of the absorber for refractive index sensing applications.

2. Structure and design

We proposed the sample of the structure of the suggested metamaterial absorber illustrated schematically in Fig. 1 to create a perfect absorber with a basic structure studied in earlier works [43,44]. Fig. 1(a) presents the simulation arrangement for the presented study. A square split ring resonator (SRR) with additional splits and four rectangular inner strips render the construction. This metamaterial structure creates the upper plane above the substrate. The square-shaped structure is 43.2 μm in width and length. As present in Fig. 1(b), other structural parameters attributed to the structure are given as $p = 39.6$ μm, $a = 12.6$ μm, $b = 14.4$ μm, $g = 3.6$ μm, $r = 3.6$ μm, $h = 2.52$ μm, $t = 0.18$ μm. The proposed unit cell uses an ITO layer over and at the back of the substrate, while the dielectric layer is lead glass. The permittivity of lead glass is 6, and its electrical conductivity is 1×10^{-12} S/m. The electrical conductivity of the ITO utilized for the top layer over the ground and the back wire is 5×10^5 S/m.

To give an expanded overview of the design process, the initial goal was to develop a perfect absorber that would operate between 1 and 5 THz. We chose a split ring resonator for the metamaterial structure that is widely used and intended for THz absorption. We added two more splits to a split ring construction along with rectangular strips that complemented to attain dual-band resonance. An extensive analysis of this modified structure's electromagnetic properties was carried out. The structure is intentionally kept symmetrical enough to ensure at least one polarization-insensitive band. A distinctive element of this research was the inclusion of optical transparency as a prerequisite. To obtain optical transparency, a transparent substrate material like lead glass was utilized. For the top conductive layer, transparent indium tin oxide (ITO) was utilized instead of metal. It provides the added benefit of tuning capabilities through doping and material characterization, which may allow fine-tuning of the absorber's performance to meet specific requirements. Incorporating a single material over the substrate highlighted the structure's simplicity. In order to simplify the material integration process and lower complexity and potential difficulties during the fabrication process, this simplified approach was chosen.

The presented design's simplicity greatly simplifies the manufacturing process, which increases its viability compared to others, as it might be challenging to obtain control over feature sizes at the micro- and nanoscale. Moreover, considering the limitations of size and strict tolerances, the exact alignment of several layers inside a complicated structure might be a crucial problem. Material compatibility is another frequent difficulty in these situations. Still, since our design only requires one material on the substrate, compatibility problems are avoided. Additionally, the production of intricate patterns poses difficulties in procedures like etching and depositing, where it becomes difficult to maintain consistency throughout the substrate. Complicated structures sometimes require complex mask production, for example, in photolithography, which presents an additional challenge. Furthermore, integrating

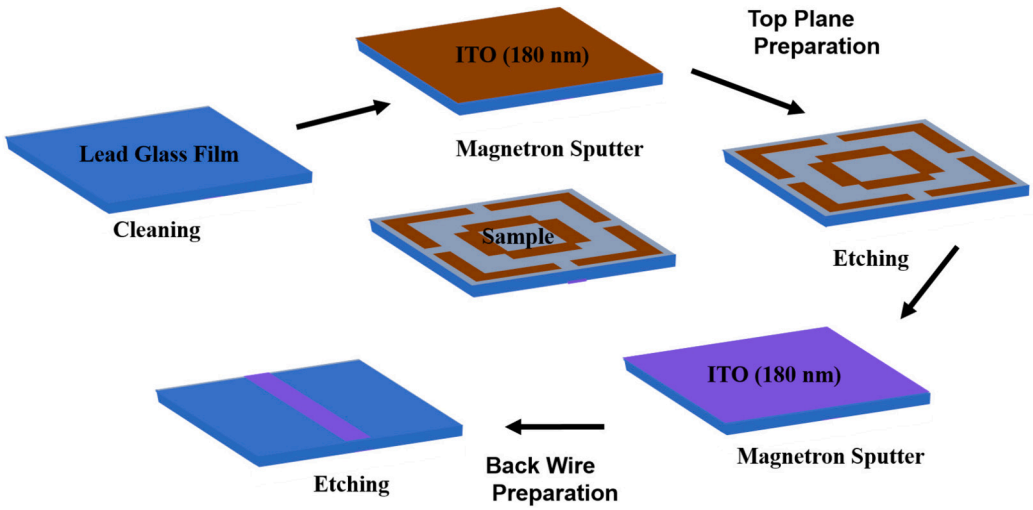

Fig. 2. Schematic image of a probable fabrication process of the proposed absorber.

multiple procedures for intricate structures can be a challenging undertaking that many production facilities may find difficult to handle. Therefore, the structure detailed here complies with most of the current technological standards.

3. Outline of the fabrication process

The proposed absorber is a thin film structure. A thin film is a layer of material with a thickness ranging from a fraction of a nanometer to several micrometers [45]. The micrometer range structures discussed here can be deposited utilizing various deposition methods such as sputtering, chemical vapor deposition (CVD), electron beam evaporation, atomic layer deposition, pulsed laser deposition, etc. We have discussed two different methods of fabricating the structure here.

3.1. Sputtering

A lead glass film can be employed as the substrate for developing the sample. This micrometer-scale thin film can be fabricated through physical vapor deposition and chemical vapor deposition, etc. Different sputtering methods, for instance, Magnetron sputtering can deposit distinct 180 nm ITO layers on both sides of this film. The wet etching method described in Fig. 2 can be utilized or traditional photolithography technology can be employed to create the resonant structure [46]. A commercial terahertz time-domain spectrometer (THs-TDS, ADVANTEST TAS7400TS) that can measure angles as small as 15 degrees can be employed to analyze the experimental study. Significantly, the observations can be carried out in a nitrogen atmosphere to remove any possible disruptions brought on by water vapor.

3.2. Inkjet printing

Inkjet Printing is an efficient technique for applying conductive layers to a lead glass film. ITO can be deposited by inkjet printing on both sides of the film [47]. Creating a layered structure with particular functions is made possible by this sequential process, which enhances the thin film's overall performance and design in potential applications.

Inkjet printing is cost-effective while sputtering allows for precise control of film thickness and uniform coatings.

4. Results and discussions

A 3D electromagnetic simulator was utilized to simulate and analyze the structure. To design a functional THz metamaterial absorber, the transmission and reflection spectra of the incident wave function must be eliminated, thus benefiting the absorber's interdependence with the occupying radiation. The frequency behavior of the absorption can be presented by equation (1).

$$A(\omega) = 1 - R(\omega) - T(\omega) \tag{1}$$

here, $A(\omega)$, $R(\omega) = |S_{11}|^2$, and $T(\omega) = |S_{21}|^2$ represent the absorbance, reflectance, and transmittance, respectively. As stated in equation (1), maximum absorption is achieved by minimizing either reflectance or transmittance or both. The imaginary components of the effective electric permittivity and magnetic permeability of the proposed metamaterial must be large to remove the transmission coefficient. This is due to the fact that these are the only variables that have an impact on metamaterial loss [48]. If the proposed absorber's absorption mechanism is discussed from an impedance-matching perspective, when considered a planar pattern, the absorber is perceived as a homogeneous dielectric material. The absorption characteristics can be stated in another form as

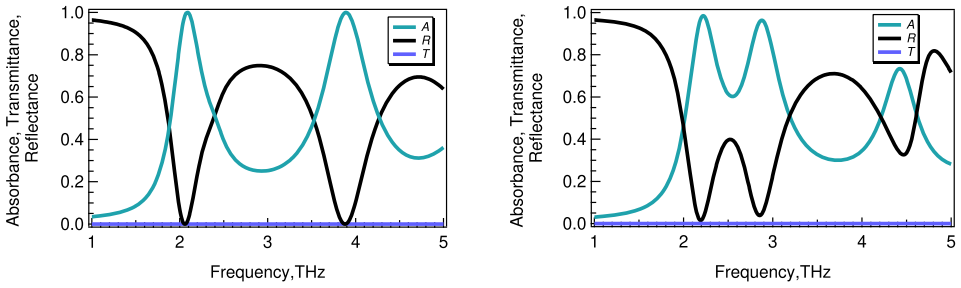

Fig. 3. (a) Absorbance, reflectance, transmittance in TE polarization mode, (b) Absorbance, reflectance, transmittance in TM polarization mode.

Table 1
Performance analysis at both frequency bands for normal incidence and normal polarization in TE and TM polarization modes.

Polarization Mode	Resonant frequency, THz	Absorption, %	FWHM, THz	Quality factor	FBW, %
TE Mode	2.089	99.99	0.5106	4.019	24.88
	3.892	99.98	0.7358	5.25	19.04
TM Mode	2.23, 2.87	98.48 (2.23 THz) 96.34 (2.87 THz)	1.1742	–	45
	4.43	73.4	0.4073	10.88	9.19

$$A(\omega) = 1 - R(\omega) = \frac{Z(\omega) - \eta_0}{Z(\omega) - \eta_0} = \frac{z(\omega) - 1}{z(\omega) + 1} \tag{2}$$

where $Z(\omega)$ is the wave impedance of the absorber, η_0 is the free space wave impedance, and $z(\omega)$ is the normalization of the wave impedance that can be estimated from S-parameters. The absorption reaches its optimum when the real part of $z(\omega)$ equals one and the imaginary portion is about zero, as shown in equation (2), indicating that the absorber's wave impedance should be adjusted to that of free space. Within the absorption spectrum, the real and imaginary parts of the normalized wave impedance oscillate about one and zero, respectively. Minor incidence wave reflections are induced by well-matched impedances, which explains the effective broadband absorption behavior in a different approach.

A metamaterial structure's reflection rate can be decreased by altering its geometrical parameters, which modify the design's characteristics and influence its impedance. When the absorption rate is high, and the reflection rate is low, the metamaterial structure's impedance at resonance frequency matches free space impedance, resulting in perfect absorption. Perfect absorption is attained when the impedance of the medium ($Z = \sqrt{\mu_r/\varepsilon_r}$) matches with the impedance of the surrounding medium ($Z_0 = \sqrt{\mu_r/\varepsilon_r}$). At that point, the wave doesn't reflect from the medium ($R(\omega) = 0$). Matched impedance is attained at two frequency bands in the proposed design.

Finite difference time-domain (FDTD) simulations based on a 3D electromagnetic simulator are utilized in obtaining the results. The unit cell structure with the electric field parallel to the z-axis is illuminated with a normally incident plane wave. The unit cell boundary condition with Floquet-port is utilized to simulate the absorption spectra. In the boundary condition setup, a unit cell boundary condition is regarded along the x and y axes, and an open boundary is considered along the z-axis.

Figs. 3(a) and 3(b) present the transmittance, reflectance and absorption spectra for the suggested metamaterial absorber in TE and TM polarization modes, respectively. Table 1 delineates absorption characteristics in both TE and TM polarization modes. The modified SRRs or sectional resonance structures used in the unit cell are strongly coupled to the electric or magnetic fields to match the impedance to free space which reduces the reflectance. Near zero reflectance $R(\omega) = |S_{11}|^2$ and transmittance $T(\omega) = |S_{21}|^2$ have been attained at two frequency bands with resonance at 2.089 and 3.892 THz in TE polarization mode, as shown in Fig. 3(a). APLF and APHF at TE polarization mode are 99.99% and 99.98%, respectively. In TM polarization mode, three bands have absorption maxima of greater than 70%. At three peak frequencies of 2.23, 2.87, and 4.43, the absorption spectra are 98.48%, 96.34%, and 73.4%, respectively, in the TM polarization mode. Dual-band perfect absorption is achieved in the TE polarization mode. At TM polarization mode, which has two near-perfect (more than 90%) absorption peaks, a broad absorption band with a fractional bandwidth of 45% is achieved, which is evident in Fig. 3(b). These two peaks can be seen at 2.23 and 2.87 THz, respectively. Another absorption peak of 73.8% was discovered at 4.43 THz. In TM polarization mode, the largest full width half maximum (FWHM) bandwidth of 1.1742 THz is attained. At perfect absorption peaks in TE polarization mode, the FWHM bandwidth is 0.5106 and 0.7358 THz, respectively, at low and high frequencies. Absorption peaks at TE polarization mode have better quality than TM polarization peaks.

Tables 2 and 3 show how the polarization angle and incidence angle affect the FWHM and Q factor of the dual-band perfect absorber, respectively. The Q-factor is defined as $Q = f_0/FWHM$ in order to explain the frequency selectivity of these absorption spectrums (f_0 is the peak frequency of an absorption band). The equivalent highest Q factor values for the specified metamaterial absorber obtained are about 14 and 35 for the 1st and 2nd absorption peaks. As a result, the suggested metamaterial absorber has a

Table 2
FWHM and quality factor variation with polarization angle variation.

Polarization		0°	10°	20°	30°	45°	60°	75°
FWHM	Peak 1	0.52	0.51	0.53	0.54	0.59	1.27	1.21
	Peak 2	0.74	0.77	0.82	0.95	1.04	0.9	0.43
Q-factor	Peak 1	4.019	4.1	3.96	3.91	3.62	1.72	1.81
	Peak 2	5.25	5.05	4.75	4.08	3.69	4.3	10.27

Table 3
FWHM and quality factor variation with incident angle variation.

Incidence		0°	10°	20°	30°	45°	60°	75°
FWHM	Peak 1	0.52	0.5	0.48	0.46	0.39	0.3	0.11
	Peak 2	0.74	0.74	0.73	0.69	0.58	0.59	0.14
Q-factor	Peak 1	4.019	4.18	4.29	4.51	5.29	6.91	14.75
	Peak 2	5.25	5.27	5.26	5.64	6.73	6.63	35.53

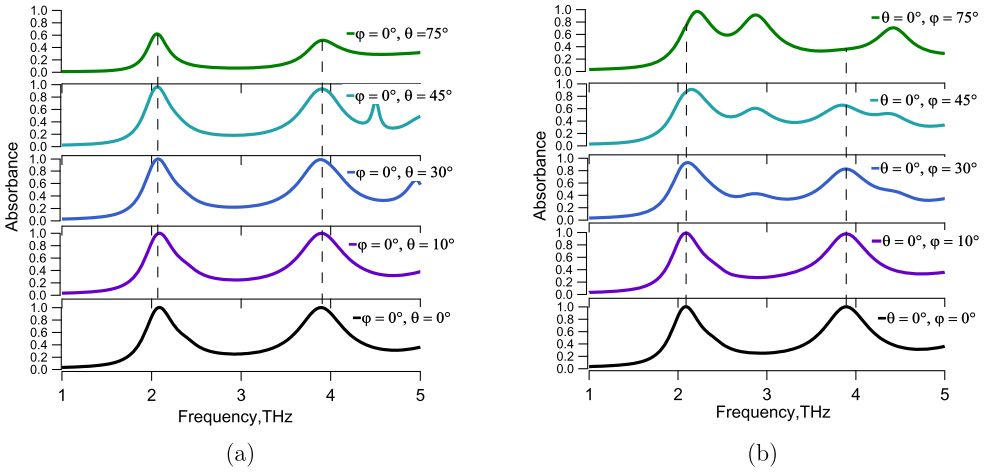

Fig. 4. Variation of absorption characteristics at both peaks with (a) incident angle variation and, (b) polarization angle variation.

much higher Q-factor than earlier ones, suggesting that it could be used for sensors or detection. Finally, we investigate the device's sensitivity to incidence and polarization. Practically, it is preferable to be independent of the incident light's polarization and to have a higher resistance to the incidence variation, since this will obviate the equipment's polarization prerequisites. The absorption spectrum is displayed for various angles of incidence and polarization within the range of 0° to 75° in order to assess the sensor's viability for practical applications. Absorption characteristics for both incident and polarization angle variation in TE polarization mode are delineated in Fig. 4.

Absorption characteristics for incident angle variation in TE polarization mode are delineated in Fig. 4(a). The two absorption peak amplitudes for TE waves remain larger than 99% for incident angles ranging from 0° to 30°. The absorption peak decreases with the rise of the angle of incidence, yet for a 60° incident angle, both low and high-frequency exhibit 81.1% and 86.5% absorption, respectively. As absorption is 99%, even around at 30° incident angle, thus, this absorber shows perfect absorption at both frequency bands as presented in Fig. 4(a). The incident magnetic flux between metal oxide layers tends to decrease as the angle of incidence increases, resulting in minimal absorption.

Absorption peak variation with alteration of polarization angle in TE polarization mode is depicted in Fig. 4(b). An unexpected spectral peak arises at roughly 2.85 THz with off-normal polarization, as seen in Fig. 4(b). This is because of a zero permeability dispersion near the frequency of magnetic plasmas. Furthermore, research suggests that the inherent dispersion of the effective parametric properties is accountable for this additional element which doesn't rely on metamaterial structure [49]. Absorption is 93.7% even at around 75° polarization angle at the first frequency band. Absorption frequency is also polarization insensitive for the first band.

By taking into account the normal incidence and polarization of the incoming wave function, all of the absorption peaks have an absorption of greater than 99% for both absorption bands, as observed. Fig. 5 depicts the change in FWHM, Q factor, and resonance frequency as a function of incident angle and polarization angle at both absorption peaks.

At the resonance frequencies of 2.089 and 3.892 THz, the surface current distribution formed by the incident electromagnetic interaction with the absorber is illustrated in Fig. 6. To better understand the metamaterial absorber's physical absorption mechanism,

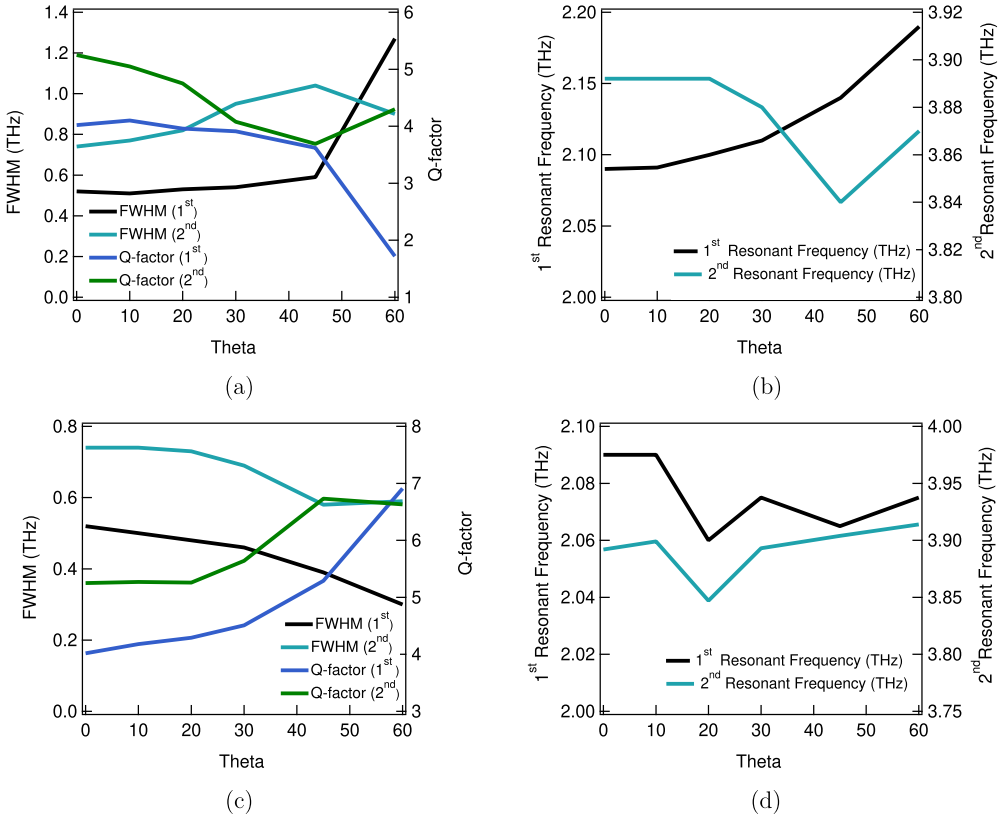

Fig. 5. (a) FWHM, Q factor, (b) Resonant frequency variation with incident angle variation, (c) FWHM, Q factor, (d) Resonant frequency variation with polarization angle variation.

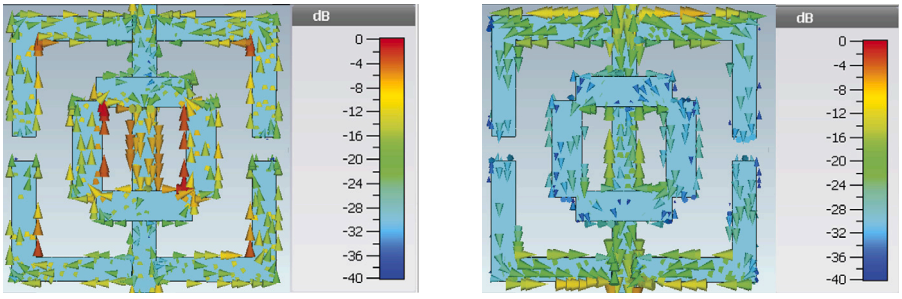

Fig. 6. Surface current distribution in TE polarization mode, (a) 2.089 THz, (b) 3.89 THz.

we assessed the surface current distribution of the top and bottom layers of the unit-cell layout at both resonances. The activation of the magnetic dipole resonance mode is evident by the development of a current loop of antiparallel currents on the top and bottom layers. Surface currents flowing in opposite directions on two metallic layers cause magnetic flux coupling with the incident H-field. Surface currents on the bottom surface are antiparallel to those on the top layer at resonance wavelength, suggesting that the absorption spectra are generated by magnetic resonance response. The surface current density is predominantly centered on ITO-based inner strips and back wire construction at the lower resonant frequency. The frequency at which the metamaterial structure exhibits the greatest absorption of electromagnetic waves is known as the resonant frequency of a metamaterial absorber. An inverse proportionality characterizes the relationship between the resonator length characterized by the top layer of the structure and resonance frequency. This phenomenon is in perfect harmony with the accepted model of the LC circuit [50], [51]. The dynamics between capacitance (C) and inductance (L) are outlined in this model. Equation (3) presents the inverse relationship between the resonance frequency and length, which reflects the expected behavior in keeping with this LC circuit model's properties.

$$f = \frac{(LC)^{-1/2}}{2\pi} \propto \frac{1}{l} \tag{3}$$

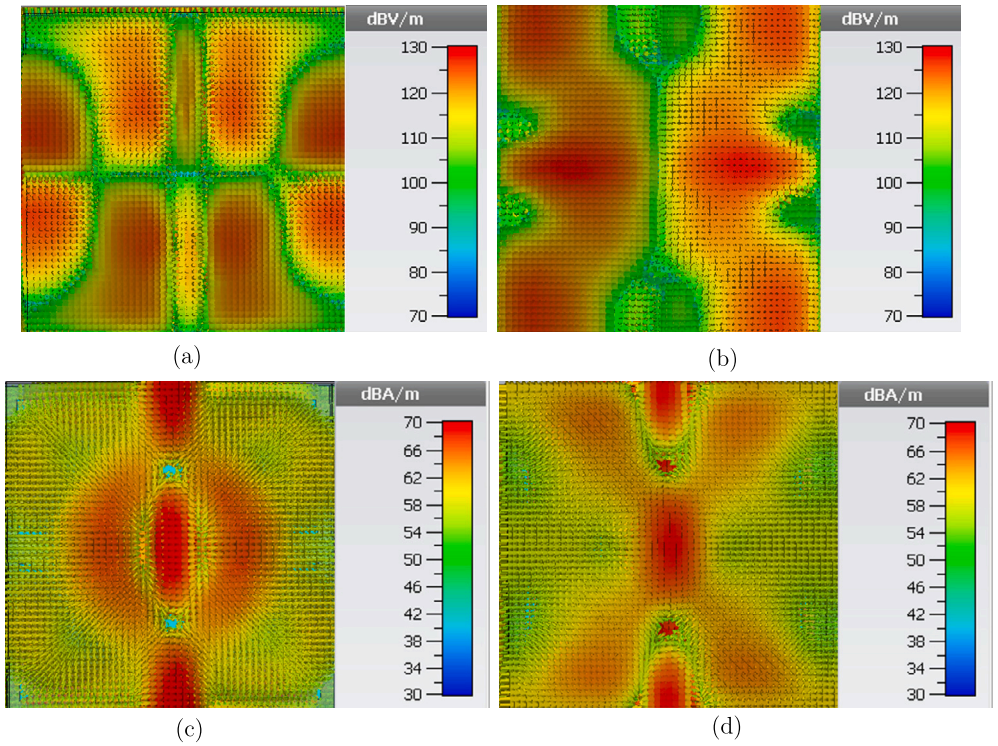

Fig. 7. Electric field distribution of the dual-band perfect absorber at (a) 2.09 THz, (b) 3.89 THz, magnetic field distribution of the dual-band perfect absorber at (c) 2.09 THz, (d) 3.89 THz.

where f is the resonant frequency and l is the length of the top split ring resonator structure. The higher resonant frequency has contributed to a fall in surface current concentration across the inner strips, with increased density at the upper and lower arms of L-shaped strips. Two sets of strong regional antiparallel current loops are produced at the lowest frequency, which indicates the excitation of the second-order (with respect to the fundamental mode) magnetic resonance condition. The top layer's induced surface currents are primarily concentrated on the left and right portions of the inner square structure formed by ITO strips, antiparallel to the back layer's induced currents. Similarly to the lower absorption peak, the generated antiparallel surface currents of the top structure are largely localized on the right and left parts of the outer and inner structure, resulting in second-order magnetic resonance, as illustrated in Fig. 6(b).

As stated before, we also research the electric field $|E|$ and magnetic field $|H|$ distributions of resonant peak 2.09 and 3.89 THz at the xy plane. Fig. 7 illustrates the electric and magnetic field distribution for both frequencies in order to fully comprehend the physics of the proposed dual-band metamaterial absorber. The first resonance frequency is mainly contributed by the resonator formed due to the space between each outer L-shaped strip and inner rectangular strip as illustrated in Fig. 7(a). In the case of the second resonant frequency shown in Fig. 7(b), the electric field is mainly localized in corners of L-shaped strips and rectangular inner strips which are not perpendicular located across the back-metal strip directly enabling the electric energy to be mainly confined in those regions. In these two circumstances, the electric field is largely concentrated in the specified zones, allowing electric energy to be restricted to those spots. It implies that because of the inclusion of the top metamaterial structure, the substrate layer captures the majority of the light, resulting in complete absorption. To gain a better understanding of the complex working principle, the simulated magnetic field $|Hz|$ at 2.09 and 3.89 THz in the xz planes are illustrated in Figs. 7(c) and 7(d). Generally, the lead glass substrate can be considered an excellent reflection cavity because of its low inherent loss, which causes lesser power loss internally and reduces the working bandwidth. This is due to the fact that lower internal loss causes light to be confined well in the cavity.

Many studies have indicated that the structural characteristics of metamaterial absorbers strongly influence their absorption efficiency, and physical defects that may develop during the manufacturing process, too, should be considered [36]. As a result, in the sections discussed below, we will look at the impact of structural parameters on the absorber's absorption capabilities one after another. We first demonstrate how the thickness of the dielectric substrate influences the structure's behavior, as presented in Figs. 8(a) and 8(b), with all the other parameters held constant. Figs. 8(a) and 8(b) illustrate how the thickness of the lead glass substrate influences the location and intensity of the device's absorption peak in different ways. The resonance bands are around peak frequencies of 2.089 and 3.892 THz. The absorption peak of high frequency (APHF) is 99.98%, and the absorption peak of low frequency (APLF) is 99.99%. At both frequencies, the dual-band absorber has near-unity absorption in TE polarization mode. The absorption spectrum of the dual-band absorber with the variation of substrate width h from 2.3 μm to 2.7 μm is illustrated in Fig. 8(a). The APLF doesn't change noticeably while the APHF reduces with the extension of h. At both peaks, a blue shift with an increase in substrate width is noticed, as illustrated in Fig. 8(a). It is discernible from Figs. 8(a) and 8(b) that when the thickness

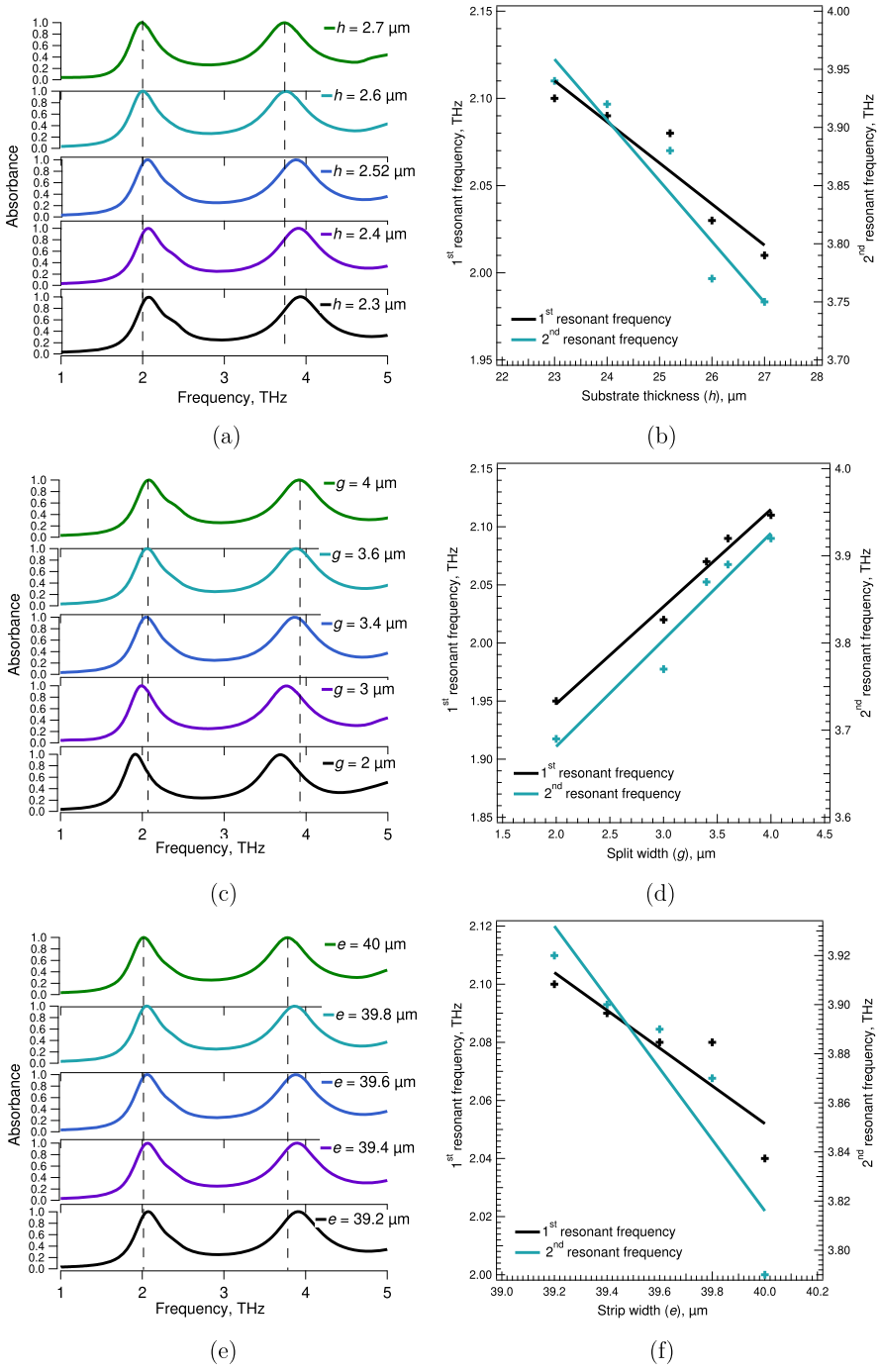

Fig. 8. Variation of resonance frequency of absorption peaks with (a), (b) substrate width, *h*, (c), (d) split width of outer structure, *g*, (e), (f) strip width of outer L-shaped structures, *e* in TE polarization mode.

of lead glass grows, the resonance wavelength shifts slightly towards the longer wave. The specifics of spectral drift and absorption level are shown in Figs. 8(a) and 8(b). It has been discovered that as the thickness of substrate width grows (from 2.3 to 2.8 μm), the position of the resonant absorption peak varies only by a few nanometers while the absorption efficiency remains essentially constant (>99%). The sensitivity of the absorption of the metamaterial structure to h can be attained by $S_h = \lambda/h$, which is 0.0236 and 0.0523 for 1st and 2nd absorption spectra, respectively. It is clear that both the operating wavelengths of the absorber are very slightly susceptible to change to the variation of h. The absorption efficiency is not influenced by the thickness of the substrate.

The sensitivity of the absorber's performance with respect to the split length, *g*, of L-shaped structures of the metamaterial unit cell is also investigated. Changing gap length, *g*, between L-shaped structures shifts both absorption peaks. When *g* is varied from

Table 4
Comparison between previous research and suggested perfect metamaterial absorber.

References	Li et al. [12]	Zhang et al. [52]	Xing et al. [53]	Yao et al. [54]	Abdulkarim et al. [55]	Proposed (TE)
Design structure	Brick	Square	Oval	Rectangular	Square	Square
Unit cell dimension, μm	2.4 × 2.4	35 × 35	2.5 × 2.5	One side 4.32	9.5 × 9.5	43.2 × 43.2
Absorption peaks	2	2	2	2	2	2
Frequency (Peak), THz	4.59	3.5–4.1	4.95	5.08	22.46	2.089
	6.18	7.15	9.2	8.56	28.95	3.892
Absorption rate,%	99.91%	90%	99.8%	97%	98.44%	99.99%
	99.31%	98.9%	99.6%	99%	99.28%	99.98%
Published year	2019	2019	2018	2016	2021	–

2 μm to 4 μm, the rightward shifts at both bands are noticeable in Figs. 8(c) and 8(d). APLF varies slightly with varying *g* with respect to second absorption resonance. APHF reduces with decreased *g*. The sensitivity of the absorption of the metamaterial structure to the split width, *g*, can be calculated by $S_g = \lambda/g$, which is 0.083 and 0.122 for the 1st and 2nd absorption spectra, respectively.

The strip width, *e*, of L-shaped structures of the absorber is the last structural characteristic we studied. Figs. 8(e) and 8(f) depict the device's relationship with the structural parameter, *e*. It shows the absorption spectra and the relationship between the resonant frequencies and the strip width. Absorption peaks after modification of L-shaped structure width from 39.2 μm to 40 μm with a span of 0.2 μm are presented in Figs. 8(e) and 8(f). As *e* increases, the resonant peak experiences a red shift, as shown in Figs. 8(e) and 8(f). The sensitivity of the absorption of the metamaterial structure to the strip width *e* can be attained by $S_e = \lambda/e$, which is 0.065 and 0.145 for 1st and 2nd absorption spectra, respectively. APLF hardly decreases with variation, but APHF decreases with increasing *e*. Both peaks show a rightward shift with extended outer structure width. Even with a slight change in *e*, the device's first resonance wavelength exhibits a more significant influence with alteration of the strip width than other structural characteristics. From all the parametric analysis, it is clear that the second resonance wavelength is more susceptible to change with parametric variation. Simultaneously, the substantial reliance of the resonance location on the structure's parametric value suggests that the device is adaptable, but this also tends to negatively influence real manufacturing. It demonstrates that it is quite susceptible to low accuracy in the manufacturing of the devices, which considerably raises the uncertainty of optimal production and simulation results significantly.

According to the findings, the size of the metamaterial substrate determines the absorber's absorption resonance characteristics, and the operating wavelength may be modified by varying the thickness of the dielectric layer and the split and strip width value of the metamaterial structure. As the absorption effectiveness is not affected by changes in structural parameters, the structural characteristics may be modified to create a tunable bandpass metamaterial absorber. The impact of the studied elements on performance metrics, like the absorber's absorption bandwidth and Q-factor, will be substantial. Those findings can also be used as a frame of comparison and a guide for test findings.

Table 4 illustrates the summary of a comparative investigation. In [12], a dual-band and polarization-insensitive metamaterials ideal absorber comprised of monolayer graphene was built and investigated in the mid-infrared region. At 4.59 and 6.18 THz, two dual-band perfect absorption peaks are observed. In this literature [52], a tunable THz metamaterial absorber with dual-band absorption comprised of a dielectric layer and a periodic combination of Au is studied. The broadband absorption rate in the 3.5–4.1 THz region can reach above 90%, and at 7.15 THz, it can approach 98.9%. In [53], adjusting the chemical potential of graphene, two perfect absorption peaks are attained. Similarly, in [54], the investigation of a dual-band perfect absorber made up of a periodical formed elliptical graphene structure with a metal ground partitioned by a thin SiO_2 dielectric layer. The structure proposed in this study has higher absorption rates in both absorption bands than all other structures discussed. Several layers of materials are also employed in [12] and [55]. However, the suggested construction only uses one material layer over the substrate. The proposed structure is simple, planar, and doesn't require tuning to attain perfect absorption.

In order to explore application areas for suggested metamaterial structure in the sensing area because of its robust ideal absorption capabilities, we investigated the relation between absorption properties and refractive index. As the refractive index of the surrounding medium increases and other parameters remain constant, the frequency of each of the absorption peak shifts leftward dramatically, as seen in Figs. 9(a) and 9(b). In Figs. 9(c) and 9(d), we look at the functional relationship of resonant wavelength shift and medium refractive index. The resonance wavelengths for various refractive indices are shown as green dots, while the black line is a linear approximation of the resonant frequency data set.

The graphs of resonance frequency vs refractive indices shown in Figs. 9(c) and 9(d) are often used to calculate the sensitivity value. As shown in equation (4), sensitivity (*S*) is defined as the ratio of shift in resonant frequency (f_0) to shift in refractive index, (*n*).

$$S = \frac{\Delta f_0}{\Delta n} \tag{4}$$

Curve fitting yields a linear relationship between the resonance frequencies and the surrounding medium's refractive index, represented by equations (5) and (6) for the 1st and 2nd absorption peaks, respectively.

$$f = -1.1099n + 3.4461 \tag{5}$$

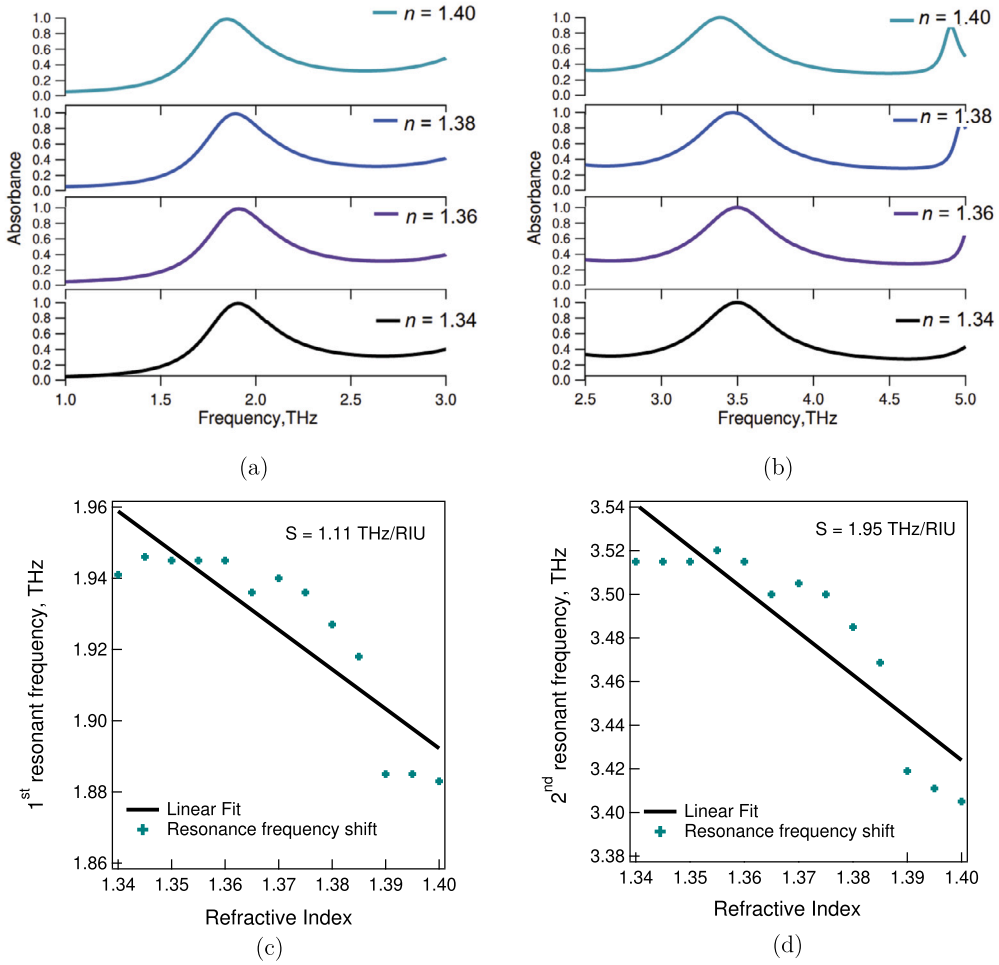

Fig. 9. (a), (b) Absorption spectra for varied refractive indices for 1st and 2nd absorption bands, (c), (d) plot of resonant frequencies versus index of refraction for 1st and 2nd absorption bands.

Table 5
Comparative analysis of the presented sensor's performance in relation of sensitivity.

References	Metal	Frequency, THz	Sensitivity (GHz/RIU)	Normalized sensitivity	RI range
[56]	Au	0.7	163	0.729	1-1.8
[41]	Au	2.249	300	0.133	1-1.39
[57]	Al	1.04	663	0.638	1.5-2.1
This work (1st)	ITO	2.089	1109	0.53	1.34-1.40
This work (2nd)	ITO	3.892	1954	0.50	1.34-1.40

$$f = -1.9544n + 6.1601 \tag{6}$$

As a result, the proposed biomedical sensor's sensitivity has been estimated to be around 1109 GHz/RIU and 1954 GHz/RIU for 1st and 2nd absorption peaks, respectively. Table 5 shows a comparison in relation to the sensitivity of similar designs considered for biomedical applications. Based on the comparison, it can be deduced that it has outstanding sensing capabilities and may be used to assess changes in the surrounding refractive index accurately.

The FOM, the percentage of the sensitivity to the FWHM of the suggested absorber presented by equation (7) [41], is another essential measure used to compare the sensing characteristics of various sensors.

$$FOM = \frac{S}{FWHM} \tag{7}$$

The highest FOM in the suggested design was discovered to be 10 and 14 for the 1st and 2nd absorption bands, respectively. Table 6 compares the presented sensor's performance with respect to the figure of merit. The proposed refractive index sensor design is

Table 6
Comparative analysis of the presented sensor's performance in relation to figure of merit (FOM).

References	FOM	Technique	Year
[58]	4	MPA integrated microfluidic channel	2016
[59]	0.5	Terahertz metamaterials	2017
[60]	7.5	Asymmetric metamaterial resonator	2018
[12]	0.85	Terahertz metamaterials	2019
[61]	0.4	Planar antenna array	2019
[41]	2.94	Terahertz metamaterial absorber	2019
[62]	0.67, 37	Terahertz metamaterial absorber	2020
[63]	1.53, 1.57	High-Q metamaterials	2020
[64]	2.94	Terahertz metamaterials	2022
This work (1st)	10	Metamaterial perfect absorber	-
This work (2nd)	14	Metamaterial perfect absorber	-

extremely sensitive regarding sensing biomedical materials. Furthermore, its high FOM makes it an outstanding sensor. With this type of sensor operating between the range of refractive indices of 1.35-1.39, the accuracy of diagnosing malignancies, carcinomas, and other disorders can be greatly increased. As a result, the study's conclusions provide benefits for a variety of detection disciplines in addition to biomedical applications. The study makes a promising advancement in MTM-based biosensing technology.

5. Conclusion

In this paper, a dual-band perfect metamaterial absorber with perfect absorption in both frequency bands is suggested. The formation of a unique metamaterial absorber that may be utilized to trace biological specimens, particularly cancerous cells, in the THz frequency range is studied and analyzed. The proposed absorber is extremely responsive to fluctuations in the surrounding medium's refractive index. When compared to similar published articles in the literature, the findings of the study were found to be superior. The results are analyzed regarding unit cell size, frequency range, absorption characteristics, polarization and incidence study, etc. Interestingly, both blood and cancerous cell organelles have refractive indices between 1.35 and 1.39, which is a smaller range. Thus, the creation of the proposed sensor with outstanding sensitivity and resolution that operates in this refractive index range has great potential for the identification of cancers, carcinomas, and other illnesses. The suggested biosensor is a functional and practical device for detecting biological materials.

Ethics declaration

No human subjects were involved in any part of the research process, and the study is concentrated on electromagnetic analysis and sensitivity performance of a THz metamaterial absorber. As a result, this study is exempt from ethical requirements pertaining to human subjects, such as informed consent and privacy protection.

CRediT authorship contribution statement

Sumaia Jahan Mishu: Writing – review & editing, Writing – original draft, Visualization, Validation, Resources, Methodology, Investigation, Formal analysis, Data curation, Conceptualization. **Muhammad Asad Rahman:** Writing – review & editing, Visualization, Validation, Supervision, Software, Resources, Formal analysis. **Nipa Dhar:** Writing – review & editing, Validation, Supervision, Software, Formal analysis.

Declaration of competing interest

The authors declare that they have no known competing financial interests or personal relationships that could have appeared to influence the work reported in this paper.

Data availability

Data will be made available on request.

References

[1] V.G. Veselago, The electrodynamic of substances with simultaneous negative values of ϵ and μ, Sov. Phys. Usp. 10 (4) (1968) 509–514, https://doi.org/10.1070/PU1968v010n04ABEH003699.

[2] J.B. Pendry, A.J. Holden, W.J. Stewart, I. Youngs, Extremely low frequency plasmons in metallic mesostructures, Phys. Rev. Lett. 76 (25) (1996) 4773–4776, https://doi.org/10.1103/PhysRevLett.87.119701.

[3] J.B. Pendry, A.J. Holden, D.J. Robbins, W.J. Stewart, Magnetism from conductors and enhanced nonlinear phenomena, IEEE Trans. Microw. Theory Tech. 47 (11) (1999) 2075–2084, https://doi.org/10.1109/22.798002.
[4] D.R. Smith, W.J. Padilla, D.C. Vier, S.C. Nemat-Nasser, S. Schultz, Composite medium with simultaneously negative permeability and permittivity, Phys. Rev. Lett. 84 (18) (2000) 4184–4187, https://doi.org/10.1103/PhysRevLett.84.4184.
[5] V.M. Shalaev, Optical negative-index metamaterials, Nat. Photonics 1 (2007) 41–48, https://doi.org/10.1038/nphoton.2006.49.
[6] W. Cai, U.K. Chettiar, H.-K. Yuan, V.C. de Silva, A.V. Kildishev, V.P. Drachev, V.M. Shalaev, Metamagnetics with rainbow colors, Opt. Express 15 (6) (2007) 3333, https://doi.org/10.1364/oe.15.003333.
[7] T.J. Yen, W.J. Padilla, N. Fang, D.C. Vier, D.R. Smith, J.B. Pendry, D.N. Basov, X. Zhang, Terahertz magnetic response from artificial materials, Science 303 (5663) (2004) 1494–1496, https://doi.org/10.1126/science.1094025.
[8] J. Huang, G. Niu, Z. Yi, X. Chen, Z. Zhou, X. Ye, Y. Tang, Y. Yi, T. Duan, Y. Yi, High sensitivity refractive index sensing with good angle and polarization tolerance using elliptical nanodisk graphene metamaterials, Phys. Scr. 94 (8) (2019) 085805, https://doi.org/10.1088/1402-4896/AB185F.
[9] T. Suzuki, M. Sekiya, T. Sato, Y. Takebayashi, Negative refractive index metamaterial with high transmission, low reflection, and low loss in the terahertz waveband, Opt. Express 26 (7) (2018) 8314, https://doi.org/10.1364/oe.26.008314.
[10] R. Dhama, B. Yan, C. Palego, Z. Wang, Super-resolution imaging by dielectric superlenses: Tio2 metamaterial superlens versus batio3 superlens, Photonics 8 (6) (2021), https://doi.org/10.3390/photonics8060222.
[11] M.R. Islam, M.T. Islam, M. Moniruzzaman, M. Samsuzzaman, H. Arshad, Penta band single negative meta-atom absorber designed on square enclosed star-shaped modified split ring resonator for S-, C-, X- and Ku- bands microwave applications, Sci. Rep. 11 (1) (2021) 1–22, https://doi.org/10.1038/s41598-021-87958-6.
[12] H. Li, J. Niu, G. Wang, Dual-band, polarization-insensitive metamaterial perfect absorber based on monolayer graphene in the mid-infrared range, Results Phys. 13 (2019) 102313, https://doi.org/10.1016/j.rinp.2019.102313.
[13] Y. Zhang, P. Wu, Z. Zhou, X. Chen, Z. Yi, J. Zhu, T. Zhang, H. Jile, Study on temperature adjustable terahertz metamaterial absorber based on vanadium dioxide, IEEE Access 8 (2020) 85154–85161, https://doi.org/10.1109/ACCESS.2020.2992700.
[14] Y. Chen, X. Pan, Z. Bao, Y. Wang, Z.D. Hu, J. Wang, Tunable terahertz perfect-absorbers with dual peak based on reverse graphene patch metamaterials, IEEE Photonics J. 13 (3) (jun 2021), https://doi.org/10.1109/JPHOT.2021.3075466.
[15] S. Banerjee, U. Nath, P. Dutta, A.V. Jha, B. Appasani, N. Bizon, A theoretical terahertz metamaterial absorber structure with a high quality factor using two circular ring resonators for biomedical sensing, Inventions 6 (4) (dec 2021), https://doi.org/10.3390/INVENTIONS6040078.
[16] N. Dhar, M.A. Rahman, M.A. Hossain, Design and exploration of functioning of a D-Z shaped SNG multiband metamaterial for L-, S-, and X-bands applications, SN Appl. Sci. 2 (1077) (2020), https://doi.org/10.1007/s42452-020-2867-0.
[17] N.T.Q. Hoa, P.H. Lam, P.D. Tung, T.S. Tuan, H. Nguyen, Numerical study of a wide-angle and polarization-insensitive ultrabroadband metamaterial absorber in visible and near-infrared region, IEEE Photonics J. 11 (1) (feb 2019), https://doi.org/10.1109/JPHOT.2018.2888971.
[18] T.S. Tuan, N.T.Q. Hoa, Numerical study of an efficient broadband metamaterial absorber in visible light region, IEEE Photonics J. 11 (3) (jun 2019), https://doi.org/10.1109/JPHOT.2019.2910806.
[19] Y. Takida, K. Nawata, H. Minamide, Security screening system based on terahertz-wave spectroscopic gas detection, Opt. Express 29 (2) (2021) 2529, https://doi.org/10.1364/oe.413201.
[20] X. Wang, CMOS fully integrated terahertz thermal detector using metamaterial absorber and proportional-to-absolute temperature sensor, Opt. Eng. 59 (9) (2020) 097106, https://doi.org/10.1117/1.OE.59.9.097106.
[21] J. Huang, J. Huang, J. Li, J. Li, Y. Yang, Y. Yang, J. Li, J. Li, J. Li, J. Li, Y. Zhang, Y. Zhang, J. Yao, J. Yao, Broadband terahertz absorber with a flexible, reconfigurable performance based on hybrid-patterned vanadium dioxide metasurfaces, Opt. Express 28 (12) (2020) 17832–17840, https://doi.org/10.1364/OE.394359.
[22] M.A. Rahman, M. Chowdhury, M.A. Hossain, A. Mobashsher, Numerical analysis of a ITO based circularly polarized optically transparent THz antenna employing characteristic mode analysis, Prog. Electromagn. Res. C 117 (2021) 1–16, https://doi.org/10.2528/PIERC21081301.
[23] M. Chowdhury, M.A. Rahman, M.A. Hossain, A. Mobashsher, A transparent conductive material based circularly polarized nano-antenna for THz applications, in: 2020 IEEE Region 10 Symposium (TENSYMP)2020 IEEE Region 10 Symposium (TENSYMP), 2020, https://doi.org/10.1109/TENSYMP50017.2020.9230696.
[24] B.-X. Wang, Y. He, P. Lou, H. Zhu, Multi-band terahertz superabsorbers based on perforated square-patch metamaterials, Nanoscale Adv. 3 (2021) 455–462, https://doi.org/10.1039/d0na00903b.
[25] N.I. Landy, S. Sajuyigbe, J.J. Mock, D.R. Smith, W.J. Padilla, Perfect metamaterial absorber, Phys. Rev. Lett. 100 (20) (2008) 1–4, https://doi.org/10.1103/PhysRevLett.100.207402, arXiv:0803.1670.
[26] H. Tao, N.I. Landy, C.M. Bingham, X. Zhang, R.D. Averitt, W.J. Padilla, A metamaterial absorber for the terahertz regime: design, fabrication and characterization, Opt. Express 16 (10) (2008) 7181, https://doi.org/10.1364/oe.16.007181, arXiv:0803.1646.
[27] M. Shahidul Islam, G. Kok Beng, N. Misran, N. Amin, M.T. Islam, A gap coupled hexagonal split ring resonator based metamaterial for S-band and X-band microwave applications, https://doi.org/10.1109/ACCESS.2020.2985845.
[28] M. Amiri, F. Tofigh, N. Shariati, J. Lipman, M. Abolhasan, Wide-angle metamaterial absorber with highly insensitive absorption for TE and TM modes, Sci. Rep. 10 (1) (2020) 1–13, https://doi.org/10.1038/s41598-020-70519-8.
[29] A. Ebrahimi, S. Barzegar-Parizi, Ultrathin, polarization-insensitive multi-band absorbers based on graphene metasurface with THz sensing application, J. Opt. Soc. Am. B 37 (2020) 2372–2381, https://doi.org/10.1364/JOSAB.396266.
[30] D. Hu, T. Meng, H. Wang, Y. Ma, Q. Zhu, Ultra-narrow-band terahertz perfect metamaterial absorber for refractive index sensing application, Results Phys. 19 (2020) 103567, https://doi.org/10.1016/j.rinp.2020.103567.
[31] J. Yu, T. Lang, H. Chen, All-metal terahertz metamaterial absorber and refractive index sensing performance, Photonics 8 (5) (2021), https://doi.org/10.3390/photonics8050164.
[32] X. Liu, T. Starr, A.F. Starr, W.J. Padilla, Infrared spatial and frequency selective metamaterial with near-unity absorbance, Phys. Rev. Lett. 104 (20) (2010) 207403, https://doi.org/10.1103/PHYSREVLETT.104.207403/FIGURES/5/MEDIUM.
[33] X. Duan, S. Chen, W. Liu, H. Cheng, Z. Li, J. Tian, Polarization-insensitive and wide-angle broadband nearly perfect absorber by tunable planar metamaterials in the visible regime, J. Opt. 16 (12) (2014) 125107, https://doi.org/10.1088/2040-8978/16/12/125107.
[34] P. Yu, H. Yang, X. Chen, Z. Yi, W. Yao, J. Chen, Y. Yi, P. Wu, Ultra-wideband solar absorber based on refractory titanium metal, Renew. Energy 158 (C) (2020) 227–235, https://doi.org/10.1016/J.RENENE.2020.05.142.
[35] M. Pan, Z. Su, Z. Yu, P. Wu, H. Jile, Z. Yi, Z. Chen, A narrowband perfect absorber with high Q-factor and its application in sensing in the visible region, Results Phys. 19 (August 2020) 103415, https://doi.org/10.1016/j.rinp.2020.103415.
[36] H. Zou, Y. Cheng, Design of a six-band terahertz metamaterial absorber for temperature sensing application, Opt. Mater. 88 (2019) 674–679, https://doi.org/10.1016/j.optmat.2019.01.002.
[37] X. Hou, X. Chen, T. Li, Y. Li, Z. Tian, M. Wang, Highly sensitive terahertz metamaterial biosensor for bovine serum albumin (BSA) detection, Opt. Mater. Express 11 (7) (2021) 2268, https://doi.org/10.1364/ome.431339.
[38] G. Qiu, Z. Gai, Y. Tao, J. Schmitt, G.A. Kullak-Ublick, J. Wang, Dual-functional plasmonic photothermal biosensors for highly accurate severe acute respiratory syndrome coronavirus 2 detection, ACS Nano 14 (5) (2020) 5268–5277, https://doi.org/10.1021/acsnano.0c02439.
[39] J.-D. Park, S. Kang, A.M. Niknejad, A 0.38 THz fully integrated transceiver utilizing a quadrature push-push harmonic circuitry in SiGe bicmos, IEEE J. Solid-State Circuits 47 (10) (2012) 2344–2354, https://doi.org/10.1109/JSSC.2012.2211156.

[40] Indium tin oxide (ITO): a promising material in biosensing technology, TrAC, Trends Anal. Chem. 97 (2017) 309–315, https://doi.org/10.1016/j.trac.2017.09.021.
[41] A.S. Saadeldin, M.F.O. Hameed, S. Member, E.M.A. Elkaramany, S.S.A. Obayya, S. Member, Highly sensitive terahertz metamaterial sensor, IEEE Sens. J. 19 (18) (2019) 7993–7999, https://doi.org/10.1109/JSEN.2019.2918214.
[42] N. Ayyanar, G. Thavasi Raja, M. Sharma, D. Sriram Kumar, Photonic crystal fiber-based refractive index sensor for early detection of cancer, IEEE Sens. J. 18 (17) (2018) 7093–7099, https://doi.org/10.1109/JSEN.2018.2854375.
[43] S.J. Mishu, R.A.K. Moushi, N. Dhar, M.A. Rahman, Design of a dual-band terahertz planar double-negative metamaterial with near zero refractive index property, in: 2021 International Conference on Science and Contemporary Technologies (ICSCT), 2021, pp. 1–6, https://doi.org/10.1109/ICSCT53883.2021.9642664.
[44] S.J. Mishu, R.A.K. Moushi, N. Dhar, M.A. Rahman, Performance analysis of a semitransparent copper based negative index metamaterial arrays, in: 2022 International Conference on Advancement in Electrical and Electronic Engineering (ICAEEE), 2022, pp. 1–5, https://doi.org/10.1109/ICAEEE54957.2022.9836374.
[45] J. Budida, K. Srinivasan, Review of thin film deposition and techniques, in: 2nd International Conference on Multifunctional Materials, Mater. Today Proc. 92 (2023) 1030–1033, https://doi.org/10.1016/j.matpr.2023.05.004.
[46] G. Shen, M. Zhang, Y. Ji, W. Huang, H. Yu, J. Shi, Broadband terahertz metamaterial absorber based on simple multi-ring structures, AIP Adv. 8 (7) (2018) 075206, https://doi.org/10.1063/1.5024606.
[47] M. Walther, A. Ortner, H. Meier, U. Loffelmann, P. Smith, J. Korvink, Terahertz metamaterials fabricated by inkjet printing, Appl. Phys. Lett. 95 (2010) 251107, https://doi.org/10.1063/1.3276544.
[48] B. Wang, T. Koschny, C.M. Soukoulis, Wide-angle and polarization-independent chiral metamaterial absorber, Phys. Rev. B, Condens. Matter Mater. Phys. 80 (3) (2009) 033108, https://doi.org/10.1103/PHYSREVB.80.033108/FIGURES/3/MEDIUM, arXiv:1005.3869.
[49] F. Zhang, Q. Zhao, L. Kang, J. Zhou, D. Lippens, Experimental verification of isotropic and polarization properties of high permittivity-based metamaterial, Phys. Rev. B, Condens. Matter Mater. Phys. 80 (19) (2009) 1–6, https://doi.org/10.1103/PhysRevB.80.195119.
[50] J. Zhou, L. Zhang, G. Tuttle, T. Koschny, C.M. Soukoulis, Negative index materials using simple short wire pairs, Phys. Rev. B 73 (2006) 041101, https://doi.org/10.1103/PhysRevB.73.041101.
[51] F. Hu, L. Wang, B. Quan, X. Xu, Z. Li, Z. Wu, X. Pan, Design of a polarization insensitive multiband terahertz metamaterial absorber, J. Phys. D, Appl. Phys. 46 (19) (2013) 195103, https://doi.org/10.1088/0022-3727/46/19/195103.
[52] Y. Zhang, C. Cen, C. Liang, Z. Yi, X. Chen, M. Li, Z. Zhou, Y. Tang, Y. Yi, G. Zhang, Dual-band switchable terahertz metamaterial absorber based on metal nanostructure, Results Phys. 14 (2019) 102422, https://doi.org/10.1016/j.rinp.2019.102422.
[53] R. Xing, S. Jian, A dual-band THz absorber based on graphene sheet and ribbons, Opt. Laser Technol. 100 (2018) 129–132, https://doi.org/10.1016/j.optlastec.2017.10.003.
[54] G. Yao, F. Ling, J. Yue, C. Luo, J. Ji, J. Yao, Dual-band tunable perfect metamaterial absorber in the THz range, Opt. Express 24 (2) (2016) 1518, https://doi.org/10.1364/oe.24.001518.
[55] Y.I. Abdulkarim, F. Özkan Alkurt, H.N. Awl, F.F. Muhammadsharif, M. Bakır, S. Dalgac, M. Karaaslan, H. Luo, An ultrathin and dual band metamaterial perfect absorber based on ZnSe for the polarization-independent in terahertz range, Results Phys. 26 (May 2021) 104344, https://doi.org/10.1016/j.rinp.2021.104344.
[56] L. Cong, R. Singh, Sensing with THz metamaterial absorbers, arXiv:1408.3711, https://doi.org/10.48550/arXiv.1408.3711, 2014.
[57] W. Zhang, F. Lan, J. Xuan, P. Mazumder, M. Aghadjani, Z. Yang, L. Meng, in: EEE MTT-S International Microwave Workshop Series on Advanced Materials and Processes for RF and THz Applications, September 2017, pp. 20–22, https://doi.org/10.1109/IMWS-AMP.2017.8247404.
[58] X. Hu, G. Xu, L. Wen, H. Wang, Y. Zhao, Y. Zhang, D.R. Cumming, Q. Chen, Metamaterial absorber integrated microfluidic terahertz sensors, Laser Photonics Rev. 10 (6) (2016) 962–969, https://doi.org/10.1002/lpor.201600064.
[59] M. Islam, S.J.M. Rao, G. Kumar, B.P. Pal, D. Roy Chowdhury, Role of resonance modes on terahertz metamaterials based thin film sensors, Sci. Rep. 7 (1) (2017) 1–8, https://doi.org/10.1038/s41598-017-07720-9.
[60] Q. Xie, G.X. Dong, B.X. Wang, W.Q. Huang, High-Q Fano resonance in terahertz frequency based on an asymmetric metamaterial resonator, Nanoscale Res. Lett. 13 (1) (2018) 1–7, https://doi.org/10.1186/S11671-018-2677-0/FIGURES/6.
[61] F. Shen, J. Qin, Z. Han, Planar antenna array as a highly sensitive terahertz sensor, Appl. Opt. 58 (3) (2019) 540–544, https://doi.org/10.1364/AO.58.000540.
[62] A. Elakkiya, S. Radha, B.S. Sreeja, E. Manikandan, Terahertz metamaterial absorber with sensing capabilities, J. Optoelectron. Adv. Mater. 22 (7–8) (2020) 360–364.
[63] Z. Liu, L. Wang, M. Hua, X. Liu, F. Qian, G. Xie, Y. Ning, Y. Shi, X. Wang, F. Yang, High-Q metamaterials based on cavity mode resonance for THz sensing applications, AIP Adv. 10 (7) (2020), https://doi.org/10.1063/5.0007590.
[64] X. Lu, H. Ge, Y. Jiang, Y. Zhang, A dual-band high-sensitivity THz metamaterial sensor based on split metal stacking ring, Biosensors 12 (7) (2022), https://doi.org/10.3390/bios12070471.